Direct observation of quantum confinement of Si nanocrystals in Si-rich nitrides

P. D. Nguyen,[1,*] D. M. Kepaptsoglou,[1,2] Q. M. Ramasse,[2] and A. Olsen[1]
[1]*Department of Physics, University of Oslo, P.O. Box 1048, Blindern, NO-0316 Oslo, Norway*
[2]*SuperSTEM Laboratory, STFC Daresbury Campus, WA4 4AD Warrington, Cheshire, United Kingdom*
(Received 6 December 2011; published 29 February 2012)

The band gap of the active layers in stacked Si-based tandem solar cells can be fine tuned by changing the size of embedded silicon nanocrystals (Si NCs). Although SiO_2 matrices have been predominantly used for such applications, nitride phases have recently emerged as a promising alternative. In this paper, we use high-resolution scanning transmission electron microscopy and energy-loss spectroscopy to report on the electronic structure of individual Si NCs embedded in silicon nitride films. Si NCs were produced by rf sputtering and exhibited controllable crystallite size and quality via different thermal annealing conditions. Quantum confinement effects were observed through a blue shift in both conduction band edges and volume plasmon energies as a function of particle size and structure. We show that, in good agreement with theoretical models, the volume plasmon energy E_p (eV) is related to the size d (nm) of Si NCs by $E_p = 16.89 + 23.90/d^2$. Lattice distortion in twinned Si NCs and dangling bonds at defect centers are shown to be the cause of a weakening in quantum size effects and a reduction in the light emission efficiency of the films. Both electron spectroscopy and optical results are consistent in explaining the correlation between structure and optoelectronic properties of Si NCs.

DOI: 10.1103/PhysRevB.85.085315 PACS number(s): 73.22.−f, 73.21.La, 73.63.Bd

I. INTRODUCTION

Over the last 10 years, the use of silicon-based tandem solar cells has emerged as a very promising technique to increase the efficiency of converting sunlight to electricity.[1] The structure of such devices involves stacks of Si-based materials with different band gap energies, which can absorb various solar spectrum bands. Carrier confinement in embedded nanoscale structures is the key to controlling the band gap of these layers. The integration of Si nanocrystals (Si NCs) with a size approaching the Bohr radius of a Si dielectric matrix allows for tuning of the band gap of the resulting material by utilizing the quantum effects related to the particle size and distribution across the solar cell.[2] The resulting quantum confined energy levels lead to an increase in the effective band gap of the nanostructure compared to bulk Si.

Extensive efforts have been made to produce the adequate structure of Si NCs embedded in a silicon oxide matrix for this type of application.[3–5] However, theoretical and experimental results recently suggested that, if silicon nitride is used as a matrix material around Si NCs, the photoluminescence peaks from the Si NCs are more blue shifted than those of similar NCs embedded in silicon oxide.[6] This enhanced energy of Si NCs in silicon nitride is attributed to the better passivation of the NCs by nitrogen atoms eliminating the strain at the Si-Si nitride interface.[6] In addition, Si_3N_4 has a lower band gap energy than SiO_2, leading to a lower barrier height and much increased carrier tunneling probability between Si NCs.[2] Therefore, Si NCs in a silicon nitride matrix are expected to be good candidates for silicon-based tandem solar cells. This nanostructure is typically formed by precipitation of Si from supersaturated silicon nitrogen solid solutions (Si-rich silicon nitride films, SRN), upon annealing at temperatures above 900 °C. Optical absorption spectroscopy and photoluminescence (PL) spectroscopy techniques have been extensively used to study the optoelectronic properties with respect to the size and structure of Si NCs embedded in silicon nitride matrix.[6–8] In spite of the fact that there have been plenty of reports on the quantum confinement-induced luminescence in this system, the origin of PL from SRN films is still an object of controversy.[9] Both the quantum confinement effects of Si NCs and defect centers, as well as the interface states in the SRN films, have been confirmed by PL measurements to give rise to the luminescence at different energy bands.[10] Although the optical techniques mentioned above have a very good energy resolution, the information they yield is averaged over a relatively large area of the specimen, which includes a large number and size distribution of NCs. Consequently, it is difficult to experimentally distinguish these mechanisms in the radiative emission. On the other hand, the very high spatial and energy resolution of dedicated aberration corrected scanning transmission electron microscopes equipped with an electron energy-loss spectrometer (STEM-EELS) provides information on the local electronic structure and elemental distribution inside the individual particles and their surrounding matrix.[11,12] To our knowledge, there has so far not been any high-spatial resolution STEM-EELS study of the quantum confinement and defect-related properties of Si NCs formed in a silicon nitride matrix.

In an attempt to explain the nanoscale origin of the PL from an electron spectroscopic point of view, we focus on using STEM-EELS to establish possible correlations between the quantum confinement of Si NCs in SRN and their size or localized defects. The size, density, and structure of Si NCs were controlled by varying the thermal annealing conditions. Changes in the band gap structure of the NCs arising from quantum confinement can be observed by shifts to higher energies (blue shift) of the volume plasmon energy or core loss edge onsets with decreasing NC size.[13,14] The relationship between structures/sizes of Si NCs and shifts in the plasmon energies and the Si $L_{2,3}$ edges will be discussed. In addition, PL suggests a strong influence of defects in Si NCs, which can act as nonradiative recombination centers and degrade the light emission efficiency. High-resolution transmission electron microscopy (HRTEM)/STEM observations, EELS,

and PL results are consistent in explaining the correlation between the structure and optoelectronic properties of Si NCs.

II. EXPERIMENT

Thin films composed of a nominally stoichiometric silicon nitride (Si_3N_4) buffer layer (∼15 nm) followed by an SRN layer (∼40 nm) were deposited on (100)-oriented single-crystal Si substrates by rf magnetron sputtering in an Ar atmosphere. The Si substrate was cleaned using a standard RCA (Radio Corporation of America) clean and given a dip in a 10% HF solution to remove the native oxide, and then dried by being blown with N_2 and put into the deposition chamber. Prior to sputtering, the chamber was evacuated to 5×10^{-7} mbar. *In-situ* Ar presputtering of the target was performed in order to remove any Si oxide on the target surface. The flow rate of Ar was maintained at a constant rate of 40 sccm during the film deposition. The excess silicon content in the SRN layer was achieved by cosputtering deposition from Si and Si_3N_4 targets at room temperature. The as-deposited layers were confirmed to be amorphous by transmission electron microscopy (TEM) imaging and electron diffraction. In order to form Si NCs in the nitride matrix, the samples were annealed in vacuum at temperatures of 900 to 1100 °C for 30 min to 2 h, depending on the specific desired nanostructure (i.e. the size and distribution of the particles within the matrix). In this paper, we report on three sets of samples that have been annealed at 1000 °C for 2 h, 1100 °C for 30 min, and 1100 °C for 2 h, hereafter denoted 1000-2 h, 1100-30 m, and 1100-2 h, respectively.

Transmission electron microscopy specimens were prepared for cross-sectional observation by mechanical polishing using the Allied MultiPrep System and finished with low-angle, Ar-ion milling at 5 keV in a Gatan PIPS 691 Precision Ion Polishing System. High-resolution transmission electron microscopy and energy-filtered transmission electron microscopy (EFTEM) observations were performed at 200 kV, with a JEOL 2010F microscope equipped with a Gatan Imaging Filter. The energy spread was determined to be ∼1.4 eV from the full width at half maximum (FWHM) of the zero-loss peak. Energy-filtered transmission electron microscopy images were acquired using the silicon bulk plasmon peak at 17 eV with an energy-slit width of 2 eV.

The STEM-EELS experiments were performed at 100 kV in a Cs-corrected Nion UltraSTEM[15] equipped with a Gatan Enfina Spectrometer. The cold field emission gun (FEG) has a native energy spread of 0.3 eV, as determined from the FWHM of the zero-loss peak in typical operating conditions. For the EELS acquisition, the collection semi-angle was 4 mrad for the low-loss datasets and 32 mrad for the core-loss datasets, and the probe convergence semi-angle was 30 mrad. In order to mitigate the effects of radiation damage and contamination on the beam-sensitive silicon nitride samples, the low-dose SMART[16] acquisition for EELS technique was employed. Postmortem images were systematically acquired in order to check for possible specimen drift during the data collection and assess specimen beam damage. Sample thicknesses in the most useful areas were determined to be 0.1 to 0.3 relative to the inelastic mean free path (t/λ) by the log-ratio method from low-loss EELS spectra. Occasionally, slightly thicker areas (up to $0.5t/\lambda$) were used when necessary in order to provide a better range of particle sizes. Due to the very low probability of plural scattering in such small thicknesses, the spectra were not treated for plural scattering removal.

III. RESULTS AND DISCUSSION

Figures 1(a) and 1(b) show, respectively, an HRTEM image and an Si plasmon EFTEM image acquired at 17 eV of the 1100-30 m sample. The observed lattice fringes in the SRN layer and electron diffraction pattern confirm the precipitation of NCs in the silicon nitride matrix. No crystallization was observed for samples annealed below 1000 °C. The EFTEM imaging at the bulk Si plasmon energy confirms that the observed NCs are indeed Si particles. The brighter areas correspond to the Si clusters and the Si substrate, while the

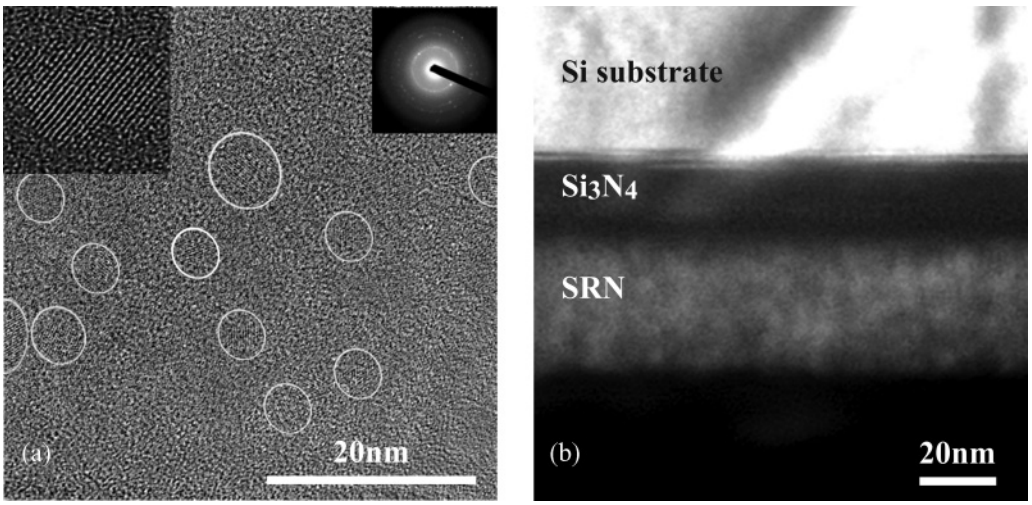

FIG. 1. (a) Cross-sectional HRTEM and (b) EFTEM at 17 eV images of Si NCs in nitride annealed at 1100 °C for 30 min. (a) shows distribution of NCs in which lattice planes can be seen clearly (left inset). Diffraction pattern (right inset) confirms crystal structure of Si particles observed by HRTEM. (b) shows layers of the film where bright areas correspond to elemental Si.

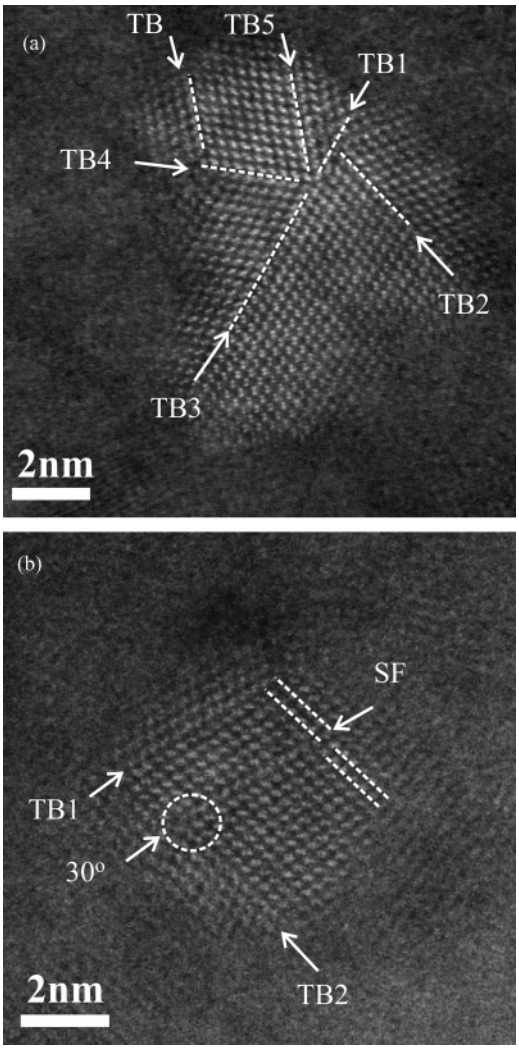

FIG. 2. (a) A HAADF STEM image of an Si NC with multiple twins and (b) a Si NC with twins, dislocation, and stacking fault in the film annealed at 1000 °C for 2 h. The arrows point out positions of twin boundaries (TB), stacking fault (SF), and a 30° partial dislocation with an extra plan marked by the dotted circle.

Si_3N_4 layer that has higher plasmon energy (∼24 eV) is dark. Delachat *et al.*[17,18] also used EFTEM imaging to identify Si NCs in a silicon nitride matrix confined between SiO_2 buffer layers and suggested that, because of the high density of NCs in their system, the phase separation mechanism probably consisted in nucleation and growth of Si NCs up to a critical size beyond which coalescence would take over. In the films grown for this study, both HRTEM and EFTEM micrographs also show that, in all samples, the amorphous SiN_x matrix contains a high density of Si NCs. However, the sizes and morphology of the Si NCs in our samples range from 1 to 30 nm and were controlled by varying the annealing temperature and/or time. The statistical analysis of the crystal size distribution obtained from the HRTEM micrographs indicates that the mean diameter and the width of the size distribution strongly depend on the annealing conditions. For instance, the mean size and the standard deviation (σ) increase with increasing the annealing temperature for the same annealing time and with increasing the annealing time for a fixed annealing temperature. Indeed, a mean size of ∼15 nm (with σ of approximately 4 nm) was observed in the 1100-2 h; the 1100-30 m and 1000-2 h exhibit finer grains, with a mean size of ∼3 nm (σ ∼ 0.8 nm) and ∼4 nm (σ ∼ 1.7 nm), respectively. While the mean sizes of Si NCs in 1100-30 m and 1000-2 h samples are comparable, in the latter, the largest particles (>5 nm) are characterized by heavy twinning (Fig. 2).

The high-angle annular dark field (HAADF) STEM image in Fig. 2(a) shows the typical morphology of twinned Si NCs observed in the 1000-2 h. We have found three- and fivefold twinned particles, with diameters as fine as about 5 nm, including twinned domains parallel to the [110] direction. Such a twinned structure has been observed before in Si NCs implanted in SiO_2 film by Wang *et al.*[19] and in silicon nitride by Delachat *et al.*,[17,18] although in the latter, the presence of these defects was not clearly linked to the NCs luminescence properties. For Si or diamond, fivefold twins with a mismatch angle of $360° - (70.53° \times 5) = 7.35°$ can be accommodated by lattice distortions or other lattice defects.[19,20] In the present work, a similar misfit was observed in Si fivefold twins; dislocations and stacking faults were also found in some NCs [Fig. 2(b)]. This indicates the presence of lattice distortion and, therefore, of electronic structure changes through dangling bonds inside these Si NCs.[21] By contrast, there is no evidence of the presence of twin defects in the Si NCs with diameters <5 nm or >20 nm (not shown), which is typically the case of the 1100-30 m and 1100-2 h samples.

The chemical state of Si particles and their surrounding matrix was investigated by core-loss EELS line scans. Figure 3(a) shows the HAADF STEM survey image of a particle in the 1000-2 h sample, where the (004) Si dumbbells are clearly resolved (probe size 0.8 Å). The HAADF image is marked with the trace of the core-loss EELS line scan taken across the particle; on average, about 70–100 spectra were acquired during each core-loss line scan. Figure 3(c) shows background-subtracted, averaged Si $L_{2,3}$ EELS spectra (each spectrum in this figure is an average of 10 adjacent spectra) from the line spectrum image in Fig. 3(b). The spectra correspond to the areas marked A to E in Figs. 3(a) and 3(b), respectively. Spectrum C in Fig. 3(c) is taken from the particle core and corresponds to the crystalline Si $L_{2,3}$ edge with a sharp onset at 99 eV and a small peak in the fine structure at 101 eV, confirming that the composition of the precipitated NC is pure Si. In the spectra from areas A and E that correspond to the SRN matrix, the Si $L_{2,3}$ edge onset remains at 99 eV as a shoulder, while a pronounced peak corresponds to Si_3N_4 present in the fine structure at 105.5 eV [marked as a vertical dotted line in Fig. 3(c)]. A similar trend has been observed in the 1100-30 m and 1100-2 h. The presence of the shoulder at 99 eV corresponding to pure Si indicates that there is a contribution from the underlying or surrounding Si particles. Given the high density of Si NCs, as shown by the HRTEM/EFTEM observation, this is a likely scenario. Spectra B and D, taken at the matrix-NC interface, resemble those in areas A and E, with a more pronounced Si shoulder at 99 eV and a broader Si_3N_4 peak in the fine structure. This reveals that the relative contribution of the pure Si edge gradually increases toward the particle core as the Si content rises.

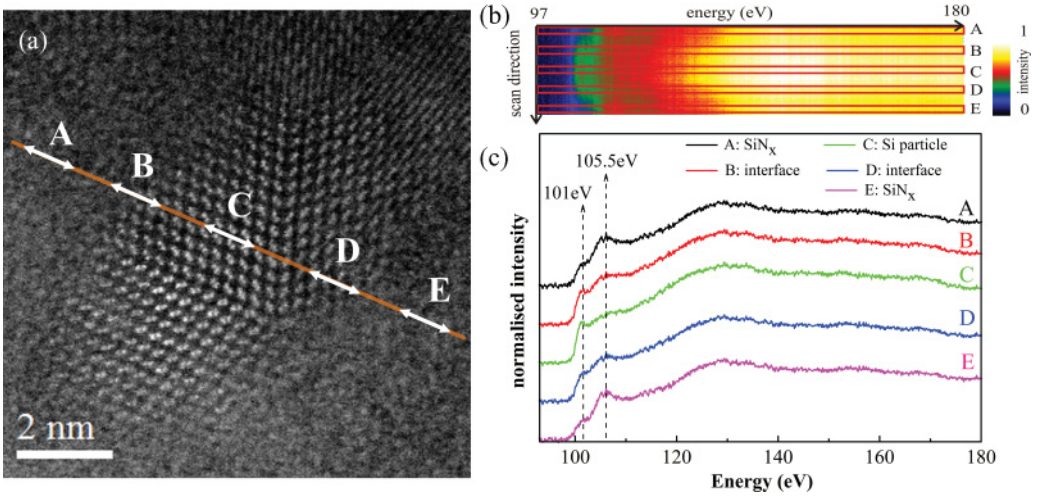

FIG. 3. (Color online) (a) A HAADF STEM image of a twinned Si NC in the film annealed at 1000 °C for 2 h, showing the trace of the Si $L_{2,3}$ edge EELS line scan. The parts of the line scan that are marked from A to E correspond to the parts of the raw spectrum image in (b) (the color scale corresponds to normalized intensity). (c) Averaged (and background subtracted) Si $L_{2,3}$ edge spectra from regions A to E, respectively.

Figure 4 shows Si $L_{2,3}$ edge EELS spectra (average of 10 adjacent spectra) taken at the cores of Si NCs of different sizes in the 1100-30 m sample. The horizontal axis corresponding to the energy loss was cross calibrated across datasets by means of the very characteristic silicon nitride peak at 105.5 eV from the matrix areas. As seen in Fig. 4, the edge shape changes dramatically as the particle size decreases from 10 to 3 nm. The edge onset gradually shifts to higher energy relative to the bulk and reaches a shift of 1.5 eV when the particle size drops to 3 nm. This behavior is similar to the observation of Batson and Heath,[13] who reported that the Si edge shape changes abruptly to a single parabolic band and a shift of 2 eV for H—terminated Si NCs smaller than 5 nm. The latter were prepared via a different method than the one used here (the gas-phase photolysis of a dilute Si_2H_6/He mixture in a gas flow cell and deposited on a holey carbon grid), albeit exhibiting a similar effect on the change of conduction band edge. Due to the lack of NCs smaller than 3 nm, the observation of quantum size effects at the Si $L_{2,3}$ edge has not been implemented in the 1000-2 h and 1100-2 h.

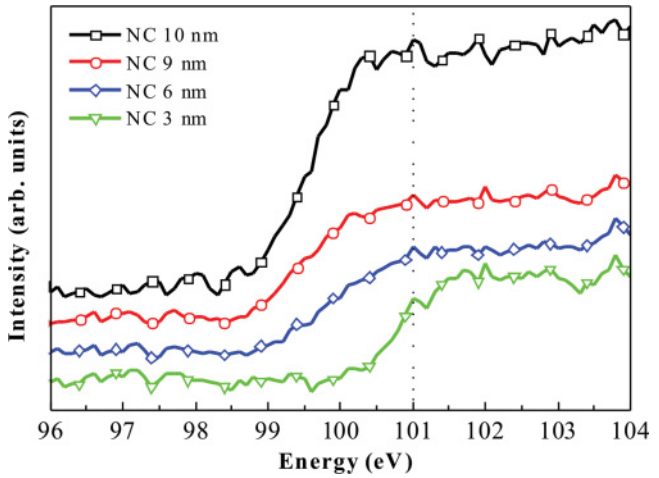

FIG. 4. (Color online) Si $L_{2,3}$ (background subtracted) EELS spectra taken at the Si NC cores with different sizes in the film annealed at 1100 °C for 30 min. The edge onset shifts and the edge shape changes with decreasing particle size. The Si peak energy at 101 eV is marked by the dot vertical line.

Figure 5 shows three distinct Si plasmon peaks acquired from Si NCs in three sets of samples. The low-loss EELS spectra presented are averaged adjacent spectra taken from a SMART acquisition linescan,[16] which was acquired in the center of the NCs. The 1100-2 h sample exhibits the narrowest plasmon peaks at 16.9 eV, of which the plasmon energy and shape correspond to that of bulk crystalline Si, confirmed in our experiment by comparison with the plasmon of the Si substrate (not shown). Plasmon peaks in the 1100-30 m are broad and have a large plateau on top, while plasmon peaks in the 1000-2 h are sharp at the lower energy side (around 17 eV) and have a shoulder at the higher-energy side (around 21 eV). It has been previously observed that, for NCs of Si, CdS, and Bi, the volume plasmon energy shifts toward higher energy, and the spectra are broadened with decreasing particle

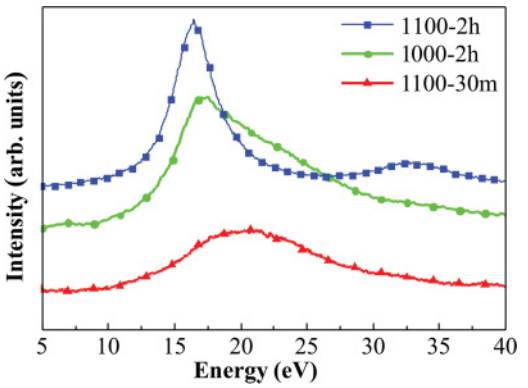

FIG. 5. (Color online) Selected low-loss EELS spectra acquired at the cores of Si NCs from samples under different annealing conditions. The shapes of the spectra are typical for each sample.

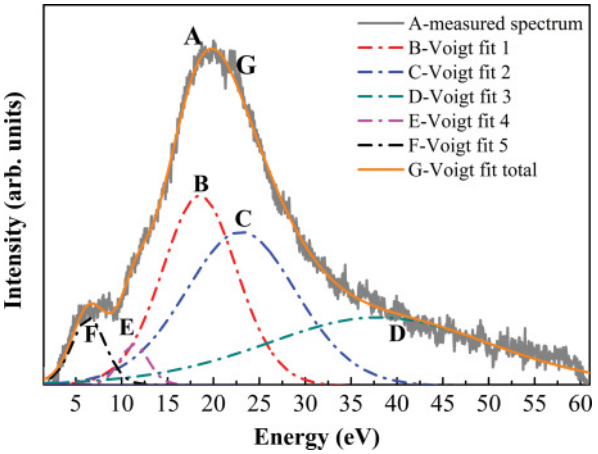

FIG. 6. (Color online) Zero-loss peak striped plasmon peak, acquired from the core of an Si NC in the film annealed at 1100 °C for 30 min. The different contributions are separated by fitting using the Voigt functional form. The first and the second Voigt peaks correspond to volume plasmon of Si NCs and their surrounding matrices, respectively.

size.[12,22,23] This is consistent with the observation in Fig. 5: the particles examined in the 1100-30 m and 1000-2 h are in the range size from 4 to 8 nm, while they are larger than 10 nm in the 1100-2 h.

Owing to the delocalized character of the plasmon excitation,[24] the sample volume contributing to the low-loss signal is significant. Therefore, the broadening of plasmon peaks of the Si NCs with small sizes is expected to contain some contribution from the vicinity of the surrounding silicon nitride matrix. The broad plasmon peaks in the low-loss EELS spectra were deconvoluted in five components using the Voigt functional form fitting method (Fig. 6). The first component corresponds to the volume plasmon of Si NCs, which were taken at the NC cores. The second component of the plasmon is the matrix contribution. Figure 7 shows the typical setting of EELS SMART acquisitions: the position of the matrix plasmon was verified independently by acquisition of low-loss EELS spectra from the matrix immediately surrounding each studied NC. The accuracy of the matrix plasmon energies depends on the density and the volume fraction of Si NCs in different samples. The determined values for the volume plasmon energies of the NCs and their adjacent matrix together with the particle size of three samples are summarized in Table I. The smaller peaks at around 5 and 10 eV correspond to the interband transition and surface plasmon energies of Si NCs, respectively.

Plasmon peaks of the matrix surrounding the Si NCs mostly have energies in the range of 20–24 eV, as seen in Table I. This indicates that the matrix is nonstoichiometric silicon nitride SiN_x ($x < 4/3$). It has been observed earlier that for silicon-rich nitride, the plasmon energy decreases from 24 to 17 eV depending on the Si excess in SiN_x.[25] The decrease of plasmon energy in SiN_x is attributed to the increase of Si-Si bond concentration. This result implies that Si agglomeration in the SiN_x films is not complete even after annealing at 1000 °C or above for a rather long time (30 min or more).

The NC size dependence of the Si volume plasmon energy was obtained, as shown in Fig. 8. The common trend in the 1100-30 m and 1000-2 h samples is that the volume plasmon energies shift toward higher energies with decrease in the particle sizes. For the former, the peak energy increases drastically when the diameter reaches ~5 nm. The blue shift of plasmon energy with decreasing the particle size attributed to the quantum size effect is described by Mitome *et al.*:[23]

$$E_P = \frac{\hbar^2 \pi^2 E_b}{\mu d^2 E_g} + E_b, \tag{1}$$

where $\hbar$ is the Planck constant, μ is the effective mass of an electron/hole pair in the material ($1/\mu = 1/m_e + 1/m_h$, where m_e and m_h are the electron and the hole effective masses, respectively), d is the particle diameter, E_p is the plasmon energy of the nanoparticle, E_b and E_g are the plasmon energy and the band gap for the bulk, respectively. This effective

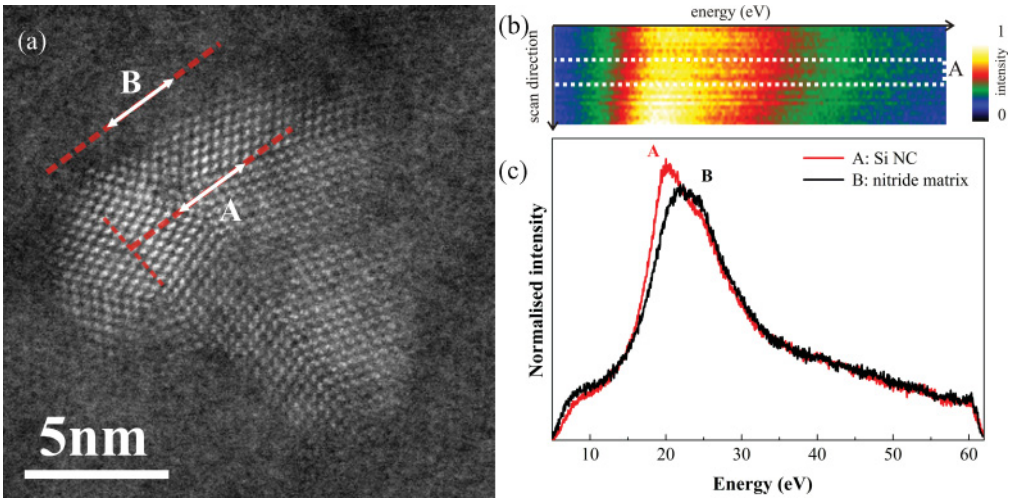

FIG. 7. (Color online) (a) The EELS SMART acquisitions for an Si nanotwin particle and its surrounding matrix in the film annealed at 1000 °C for 2 h. (b) The spectrum image of the SMART acquisition on the Si particle, where A corresponds to the line scan at the particle core (the color scale corresponds to normalized intensity). (c) Si NC and matrix plasmons from regions A and B in (a).

TABLE I. Plasmon energies of different size Si NCs and their surrounding matrices.

Sample	Particle diameter (nm)	Volume plasmon energy of Si NC (eV)	Plasmon energy of silicon nitride matrix (eV)	FWHM of Si volume plasmon peaks (eV)
1000-2 h	6.6 (twin)	17.33	20.36	3.22
	6.9 (twin)	17.38	20.10	3.64
	7.0 (twin)	17.36	20.10	4.11
	7.5 (twin)	17.20	19.90	4.36
	8.0	17.13	20.20	4.03
	8.9 (twin)	17.03	20.20	3.74
1100-30 m	3.8	18.56	23.85	9.82
	4.3	18.20	22.79	9.32
	5.2	17.80	23.03	8.73
	5.5	17.64	22.33	8.11
	5.6	17.60	20.10	5.90
	6.6	17.52	20.86	4.47
	7.0	17.34	21.31	3.22
	7.7 (twin)	17.33	20.10	3.82
1100-2 h	11.0	16.94	21.14	3.80
	20.4	16.90	20.10	3.51

mass model predicts the relationship between the particle size and its plasmon energy $E_P \approx 1/d^2$. The observed increasing volume plasmon energy of Si NCs in the 1100-30 m sample agrees well with predictions from this model as seen in the inset of Fig. 8. The rise of the volume plasmon energy in NCs of a semiconductor is known to be a result of the band gap expansion in the excitonic quantum confinement regime, which becomes significant at sizes smaller than the Bohr radius of bulk crystalline Si (around 5 nm). The experimental data of the 1100-30 m sample are best fitted by the equation:

$$E_p = 16.89 + 23.90/d^2, \tag{2}$$

plotted as the dotted line in Fig. 8. An energy shift $\delta E_p = 0.4$–1.6 eV with respect to the bulk plasmon energy of 16.9 eV is thus obtained for a NC size range of 3.8–7.7 nm in this sample. A similar shift measured by x-ray photoelectron spectroscopy was reported by Mannella *et al.* for porous Si with sizes of 2.4–3.4 nm.[26] From Eq. (2), an effective mass $\mu = 0.47m_0$ was estimated, where m_0 is the electron rest mass. This effective mass is much smaller than the reported value of $1.1m_0$ for freestanding Si nanoclusters obtained by Mitome *et al.*,[23] suggesting that the quantum confinement effect is stronger in our system. Nevertheless, this value is very close to that obtained in c-Si ($\mu = 0.48m_0$ at 300 K) by Barber[27] and a-Si/SiO_2 quantum wells by Lockwood *et al.*[28] These results imply the importance of the sample preparation method, which leads to different surface chemistry and shapes of Si NCs. For instance, Si clusters prepared by using SiH_4 as a precursor gas in Ref. 23 might be terminated by amorphous layers of polysilane around the clusters,[23] whereas our Si NCs are passivated by nitrogen. Additionally, the freestanding Si clusters reported in Ref. 23 were spherical in shape, while in our case, they are nonspherical and have

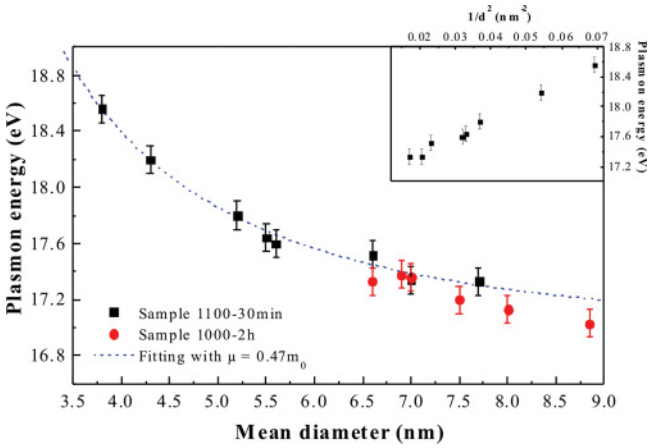

FIG. 8. (Color online) Size dependence of the plasmon energy in the 1100-30 m and 1000-2 h samples. The dot line is the least squares fit by effective mass theory to the data of the 1100-30 m. The inset shows the increase of plasmon energy proportional to the inverse square of particle diameter $E_P \approx 1/d^2$ in the 1100-30 m sample.

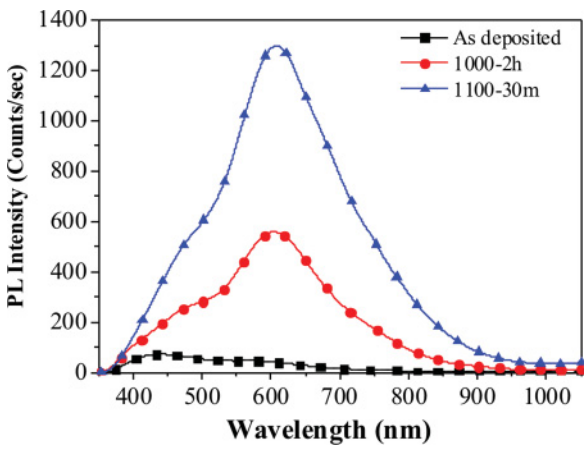

FIG. 9. (Color online) The PL spectra of the 1100-30 m, 1000-2 h, and as-deposited samples. Both the 1100-30 m and 1000-2 h exhibit a PL maximum centered at around $\lambda = 605$ nm (2.05 eV) with a small shoulder at $\lambda = 480$ nm (2.6 eV).

irregular morphologies, hence the confinement is expected to be stronger in some dimensions than others.

While the 1100-30 m sample provides data that fit nicely into the effective mass curve, the plasmon energy as a function of Si NC size in the 1000-2 h is systematically shifted down on the energy scale by approximately 0.2 eV. The fact that most of the particles examined in this latter sample include twins or other defects is a very likely reason for the weakening of the observed plasmon energy shift compared with similar-sized, defect-free particles in the 1100-30 m. A shift of ∼0.4 to 0.9 eV in plasmon energies due to lattice distortion in c-ZrO_2/α-Al_2O_3 has been reported by Yamada *et al.*[29] The decrease in plasmon energy of α-Al_2O_3 by 0.9 eV in that system was attributed to a 6% lattice expansion. The presence of lattice distortion, stacking faults, and dislocations inside the Si-twinned unit cells, as mentioned above, could thus alter the charge density and in turn change the plasmon energies. The observed downward shift in plasmon energies due to stacking faults and dislocations appears to be higher than the shift due to twinning effect, as evidenced by results obtained on a particle with a diameter of ∼6.6 nm. In this particle [Fig. 2(b)], the line scan was acquired close to a dislocation core and across a stacking fault. Although additional data would be required to confirm it, this observation is in good agreement with the report by Hanrath and Korgel that stacking faults strongly attenuate the plasmon signal of Ge nanowires.[30] Calculation of lattice distortions by using plasmon energy shift could further confirm this hypothesis. It is worth mentioning that the Si NCs in the 1100-2 h sample exhibit no remarkable blue shift at volume plasmon energies, which is expected since the sizes of these NCs are much larger than the quantum confined size range.

The combined observation of a blue shift of the plasmon energies and a shift of up to 1.5 eV in the core-loss Si $L_{2,3}$ edge onset of the particle as small as 3 nm (sample 1100-30 m) provide conclusive evidence of the presence of confinement effects in Si NCs within Si-rich nitrides. We attribute this blue shift to a specific quantum confinement effect, which raises the energy of the bottom of the conduction band relative to the Si $2p$ core level. This hypothesis agrees with the EELS data and conclusions from Batson and Heath[13] for H-terminated Si NCs with sizes <5 nm or from Sun *et al.*[31] for Si nanowires of 2.5 nm. Furthermore, the strong dependence of the observed blue shift on the size of the Si NCs fits very well within the general theoretical framework established by Delerue *et al.*[32] Using first-principles calculations, they estimated the recombination rate of electron-hole pairs in Si nanostructures and found that the balance between the size dependence of radiative and nonradiative events leads to the prediction of a blue shift of the luminescence for small crystallites. Indeed, our results are also in very good agreement with the PL energy shifts observed, for instance, for crystalline Si quantum dots embedded in silicon nitride reported by Kim *et al.*[7]

In addition to the electronic properties discussed above, the presence of defects in semiconductor crystals can strongly influence the electrical and optical properties of the material.[21,33] To relate luminescence properties with the nanostructure of Si NCs, the PL spectra of the 1100-30 m and 1000-2 h samples were measured and analyzed. Figure 9 compares the PL spectra from three samples: 1100-30 m, 1000-2 h, and as-deposited, excited at 325 nm by an ultraviolet PL spectroscopy at room temperature. The as-deposited film does not show any appreciable light emission, while the other two exhibit a strong PL maximum centered at around $\lambda = 605$ nm (2.05 eV), with a small shoulder at $\lambda = 480$ nm (2.6 eV), as shown in Fig. 9. These are in excellent agreement with the results and quantum confinement modeling obtained from Si NCs with a core diameter of 3 nm reported by Ledoux *et al.*[34]

A significantly lower PL intensity was obtained in the 1000-2 h sample compared to that in the 1100-30 m. The heavier defect density present in the 1000-2 h is evidently responsible for the large drop in PL intensity compared to that of the defect-free Si NCs in the 1100-30 m, which is in agreement with our STEM-EELS observations. Dangling bonds at dislocations can introduce extra electronic states in the band gap, which are referred to as intraband gap states and tend to trap carriers.[35] Furthermore, as the calculations of Delerue *et al.*[32] show, if these energy states are lying near the center of the band gap, they may be capable of trapping either electrons or holes and, hence, act as nonradiation recombination centers, which cause the decrease in light emission efficiency. Surface states in the Si NCs do not appear to play a major role, since the average particle sizes in both samples are comparable. These results clearly demonstrate the significant impact of crystal imperfections on the optical emission from Si NCs. Moreover, the PL results shown here provide strong support for our previous explanation of the weakening of quantum confinement effects in the 1000-2 h sample.

Finally, we briefly comment on the mechanisms of twin growth in Si NCs, for which temperature and time are crucial factors. If twinned NCs are formed by coalescence of small Si NCs, one would expect that the smaller crystals (<4 nm) are twin free because they have not grown to an impingement size.[36] Certainly, some rearrangements of the crystals are necessary before the crystal merging to get a twin relation. The twinned structure is unstable due to its higher free energy compared to twin-free structure. Twin boundaries do raise the energy of the system and should be considered as defects. The observation that big NCs (∼20 nm) are twin free indicates that, when given enough time, the system will lower its free energy by reconstructing and transforming into large twin-free particles. Annealing at 1100 °C for 30 min gives Si NCs with small grain size and size distribution, very few of which are twins. Annealing at 1100 °C for 2 h gives enough time for grain growth to reach a size where most of the crystals are without twins. Indeed, in the 1100-2 h sample, there is very little evidence of twins. Our argument until this point has been restricted to 1100 °C, where the atoms have sufficient diffusion rate to find their best positions in order to grow crystals without twinning at 1100 °C. At the lower temperature of 1000 °C for 2 h, however, the atoms have less mobility and are more likely to be trapped by one another, giving rise to an increase of twinned defects. This explains the higher density of twinning in the 1000-2 h compared to that in the 1100-30 m.

IV. CONCLUSION

We have demonstrated that the size, density, and structure of Si NCs embedded in a silicon nitride matrix can be controlled by varying the thermal annealing conditions. The

HRTEM/EFTEM analysis shows that the mean size and size distribution of Si NCs increase with increasing the annealing temperature for the same annealing time, and with increasing the annealing time for a fixed annealing temperature. The STEM-EELS and distributed dose (SMART) techniques were applied to this system to carry out a comprehensive study of quantum confinement effects as a function of the size and morphology of the Si NCs and are in qualitative agreement with carrier quantum confinement theory. The observation of twinning and defects in Si NCs and their impact on the blue shift of plasmon energy and PL intensities suggests a strong impact of crystal imperfections in the luminescence process of Si NCs. High-quality materials are needed in order to eliminate the nonradiative recombination and engineer the required band structure. Our direct evidence of quantum confinement in this system confirms the viability of Si-rich nitride as a matrix for nano-structured thin films in tandem solar cell stacks and opens up promising avenues for the exploitation of the higher band gap energy of SiN_x in photovoltaic applications.

ACKNOWLEDGMENTS

The authors would like to thank the University of Oslo for financial support. Phuong Dan Nguyen would like to thank Ole Bjørn Karlsen for useful discussions and for assistance with sample preparation. We also thank Augustinas Galeckas and Lars Olav Vestland for carrying out the PL measurements.

*Corresponding author: danpn@fys.uio.no

[1] M. A. Green, Prog. Photovolt: Res. Appl. **9**, 123 (2001).
[2] G. Conibeer, M. A. Green, D. König, I. Perez-Wurfl, S. Huang, X. Hao, D. Di, L. Shi, S. Shrestha, B. Puthen-Veetil, Y. So, B. Zhang, and Z. Wan, Prog. Photovolt: Res. Appl. **19**, 813 (2011).
[3] H. Tamura, M. Ruckschloss, T. Wirschem, and S. Veprek, Appl. Phys. Lett. **65**, 1537 (1994).
[4] N. Daldosso, M. Luppi, S. Ossicini, E. Degoli, R. Magri, G. Dalba, P. Fornasini, R. Grisenti, F. Rocca, L. Pavesi, S. Boninelli, F. Priolo, C. Spinella, and F. Iacona, Phys. Rev. B **68**, 085327 (2003).
[5] L. Pavesi, L. Dal Negro, C. Mazzoleni, G. Franzò, and F. Priolo, Nature **408**, 440 (2000).
[6] M. S. Yang, K. S. Cho, J. H. Jhe, S. Y. Seo, J. H. Shin, K. J. Kim, and D. W. Moon, Appl. Phys. Lett. **85**, 3408 (2004).
[7] T. W. Kim, C. H. Cho, B. H. Kim, and S. J. Park, Appl. Phys. Lett. **88**, 123102 (2006).
[8] P. RJ Wilson, T. Roschuk, K. Dunn, E. N Normand, E. Chelomentsev, O. HY Zalloum, J. Wojcik, and P. Mascher, Nanoscale Res. Lett. **6**, 168 (2011).
[9] J. Kistner, X. Chen, Y. Weng, H. P. Strunk, M. B. Schubert, and J. H. Werner, J. Appl. Phys. **110**, 023520 (2011).
[10] M. Wang, D. Li, Z. Yuan, D. Yang, and D. Que, Appl. Phys. Lett. **90**, 131903 (2007).
[11] P. R. Coxon, Y. Chao, B. R. Horrocks, M. Gass, U. Bangert, and L. Šiller, J. Appl. Phys. **104**, 084318 (2008).
[12] N. D. Browning, M. F. Chisholm, and S. J. Pennycook, Nature **366**, 143 (1993).
[13] P. E. Batson and J. R. Heath, Phys. Rev. Lett. **71**, 911 (1993).
[14] Y. W. Wang, J. S. Kim, G. H. Kim, and K. S. Kim, Appl. Phys. Lett. **88**, 143106 (2006).
[15] O. L. Krivanek, G. J. Corbin, N. Dellby, B. F. Elston, R. J. Keyse, M. F. Murfitt, C. S. Own, Z. S. Szilagyi, and J. W. Woodruff, Ultramicroscopy **108**, 179 (2008).
[16] K. Sader, B. Schaffer, G. Vaughan, R. Brydson, A. Brown, and A. Bleloch, Ultramicroscopy **110**, 998 (2010).
[17] F. Delachat, M. Carrada, G. Ferblantier, A. Slaoui, C. Bonafos, S. Schamm, and H. Rinnert, Physica E **41**, 994 (2009).
[18] F. Delachat, M. Carrada, G. Ferblantier, J. J. Grob, and A. Slaoui, Nanotechnology **20**, 415608 (2009).
[19] Y. Q. Wang, R. Smirani, and G. G. Ross, Nano Lett. **4**, 2041 (2004).
[20] X. Jiang and C. L. Jia, Appl. Phys. Lett. **80**, 2269 (2002).
[21] J. E. Northrup, M. L. Cohen, J. R. Chelikowsky, J. Spence, and A. Olsen, Phys. Rev. B **24**, 4623 (1981).
[22] P. N. H. Nakashima, T. Tsuzuki, and A. W. S. Johnson, J. Appl. Phys. **85**, 1556 (1999).
[23] M. Mitome, H. Yamazaki, H. Takagi, and T. Nakagiri, J. Appl. Phys. **72**, 812 (1992).
[24] R. F. Egerton, *Electron Energy—Loss Spectroscopy in the Electron Microscope* (Plenum Press, New York and London, 1986), p. 131 .
[25] V. A. Gritsenko, H. Wong, J. B. Xu, R. M. Kwok, I. P. Petrenko, B. A. Zaitsev, Yu. N. Morokov, and Yu. N. Novikov, J. Appl. Phys. **86**, 3234 (1999).
[26] N. Mannella, G. Gabetta, and F. Parmigiani, Appl. Phys. Lett. **79**, 4432 (2001).
[27] H. D. Barber, Solid State Electron. **10**, 1039 (1967).
[28] D. J. Lockwood, Z. H. Lu, and J. M. Baribeau, Phys. Rev. Lett. **76**, 539 (1996).
[29] S. Yamada, J. Ohta, and H. Kusanagi, J. Appl. Phys. **88**, 5206 (2000).
[30] T. Hanrath and B. A. Korgel, Nano Lett. **4**, 1455 (2004).
[31] X. H. Sun, Y. H. Tang, P. Zhang, S. J. Naftel, R. Sammynaiken, T. K. Sham, H. Y. Peng, Y.-F. Zhang, N. B. Wong, and S. T. Lee, J. Appl. Phys. **90**, 6379 (2001).
[32] C. Delerue, G. Allan, and M. Lannoo, Phys. Rev. B **48**, 11024 (1993).
[33] P. E. Batson, Phys. Rev. B **61**, 16633 (2000).
[34] G. Ledoux, J. Gong, F. Huisken, O. Guillois, and C. Reynaud, Appl. Phys. Lett. **80**, 4834 (2002).
[35] J. Nelson, *The Physics of Solar Cells* (Imperial College Press, London, 2003), p. 211.
[36] Y. Q. Wang, R. Smirani, G. G. Ross, and F. Schiettekatte, Phys. Rev. B **71**, 161310R (2005).